Design of Induction Motors With Flat Wires and Copper Rotor for E-Vehicles Traction System

Mircea Popescu, *Fellow, IEEE*, Lino Di Leonardo, Giuseppe Fabri, *Member, IEEE*, Giuseppe Volpe, *Member, IEEE*, Nicolas Riviere, and Marco Villani

***Abstract*—This paper deals with the design of a 200 kW/ 370 Nm, induction machine for electrical vehicles traction system. The design aims to enhance the performance of the current induction machine technology for mass production making it suitable to be a rare earth free solution for electric vehicle applications. To this extent, suitable materials have been analyzed and selected, also by using of mechanical analysis and experimental data. Rotor die-casting, hairpin stator winding and specific cooling systems have been adopted within the proposed solutions. Extensive analytical and numerical methods are used for performance evaluation all over the full speed range of the machine.**

***Index Terms*—Cooling, copper alloys, dynamic response, induction motors, losses, steel, traction motors, vehicles, windings, wire.**

I. Introduction

INDUCTION motor (IM) is the leading technology in many industrial applications, nevertheless, suitable IM designs are proposed even for automotive applications [1] where other technologies based on rare earth (RE) Permanent Magnets (PM) are usually preferred, [2], [3], [4], [5], [6]. The current geopolitical situation and the envisioned growth in the production of EVs arise concerns in the supply chain of RE PM [7], [8].

Therefore, researchers have been looking for PM motor alternatives to explore powerful, efficient, lighter, compact, and cost-effective motor solutions, [9], [10], [11].

The induction machine is considered a potential candidate because no RE materials are adopted, envisioning mass production at a lower cost and with reduced risk on the supply chain.

Manuscript received 10 December 2020; revised 29 June 2021, 1 February 2022, and 3 February 2023; accepted 25 February 2023. Date of publication 14 March 2023; date of current version 19 May 2023. Paper 2020-TSC-1593.R3, presented at 2019 Energy Conversion Congress & Exposition (ECCE), Baltimore, MD, USA, Sep. 29–Oct. 3, 2019, and approved for publication in the IEEE Transactions on Industry Applications by the Transportation Systems Committee of the IEEE Industry Applications Society. This work was supported by Horizon 2020, GV04 Program through Project ReFreeDrive under Grant 770143. *(Corresponding author: Marco Villani.)*

Mircea Popescu and Nicolas Riviere are with Ansys, S1 2JE Sheffield, U.K. (e-mail: mirceap@ieee.org; nicolas.riviere@ansys.com).

Lino Di Leonardo, Giuseppe Fabri, and Marco Villani are with the Department of Industrial and Information Engineering and Economics, University of L'Aquila, I-67100 L'Aquila, Italy (e-mail: lino.dileonardo@univaq.it; giuseppe.fabri@univaq.it; marco.villani@univaq.it).

Giuseppe Volpe is with Magna Powertrain, Troy, MI 48083 USA (e-mail: giuseppe.volpe@magna.com).

Color versions of one or more figures in this article are available at https://doi.org/10.1109/TIA.2023.3256391.

Digital Object Identifier 10.1109/TIA.2023.3256391

TABLE I
Motor Requirements

Requirement	Unit	Value (Tesla IM)	Target Value (CR- IM)
Peak power	kW	225	>200
Peak torque	Nm	430	>350
Maximum speed (target)	rpm	14500	>20000
Nominal torque	Nm	172	>150
Nominal power	kW	90	>70
Peak specific power*	kW/kg	3.31	>4.3
Peak specific torque*	Nm/kg	6.32	>8.2
Peak power density*	kW/l	19.75	>22
Rated power density*	kW/l	7.9	>8
Efficiency	%	92	≥ 94
Maximum DC bus voltage	V	400	720
Maximum phase current	Arms	636	500
Maximum available size	mm	n/a	240x240x310

(*) active materials only.

Even if IM presents a lower efficiency and torque density than PM motors, the technology is well-established in the automotive industry, and it still represents an attractive and feasible solution for EVs. The main reasons are its simplicity, robustness, versatility, cost-effectiveness, manufacturing aspects, and fault-tolerant capabilities, [12], [13], [14], [15].

In addition, a copper rotor is usually preferred to aluminum due to its higher electrical conductivity, higher mechanical strength, and better thermal properties, [16]. The rotor can be either die-cast or fabricated and both methods are now industry proven, [17], [18], [19], [20]. The IM was adopted in Tesla and Audi series-produced electric vehicles, featuring a copper and an aluminum rotor respectively, [21].

The aim of the presented study is to propose a high-performance Copper Rotor Induction Motor (CR-IM) where the combination of a high-speed liquid-cooled copper rotor and a stator with hairpin-winding are suitable for premium vehicle applications overcoming the performance of the Tesla Model S 60D motor. In addition to [1], details on the design flow, on the prototype, and extensive efficiency analysis of the machine are provided. The control scheme including simulated and experimental dynamic performances is also presented in this paper to complete the discussion.

In detail, the requirements and the technical choices adopted, and the material selected for the final design are discussed respectively in Sections II and III.

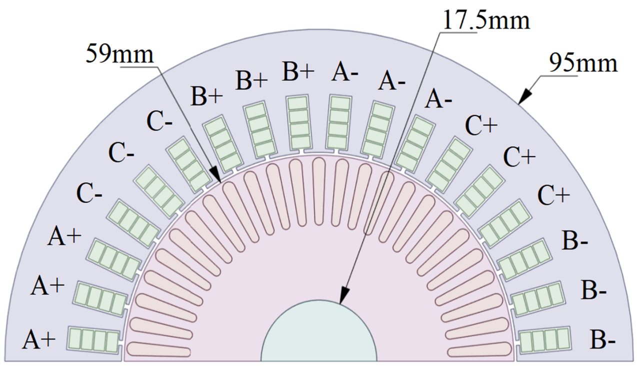

Fig. 1. Radial cross sections of proposed CR-IM designs.

Section IV presents the analysis of the electromechanical performance in terms of torque-speed characteristics and efficiency maps, with a focus on the losses in the windings due to the current harmonics.

Section V details the cooling aspects, and Section VI validates dynamically the motor performance before drawing conclusions.

II. Machine Topology

The motor requirements are reported in Table I. The key performance indicators, including efficiency, specific torque, specific power, and power density are defined. The target values are based on the Tesla Model S 60D motor ([22], [23]) plus additional boundary conditions envisioned by considering a Jaguar Land Rover Premium vehicle as a reference.

A hairpin winding is used on the stator side [24], [25]. The proposed design for the CR-IM uses the unique performance of the proprietary hairpin stator winding developed by Tecnomatic SpA, [26]**.** In contrast to conventional round wire windings, the hairpin stator winding uses precision-formed rectangular wires. Multiple layers of interlocking "hairpins" produce a superior slot fill factor (up to 73% vs. 40% for typical round-wire windings) [27], [28]. Nevertheless, the large cross-sectional area of the conductors may cause high eddy current losses (i.e., skin and proximity effects), in particular when high fundamental frequencies are used (at high speed) or current harmonics are introduced by the Pulse Width Modulation (PWM), [29], [30], [31].

From a thermal perspective, the machine will be stator and rotor cooled and two different solutions are investigated. The first one consists of a conventional water jacket housing with a spiral groove shaft Cooling System (CS), using a mixture of ethylene, water, and glycol mixture as a coolant. The second one is equipped with a spray cooling system with nozzles on the housing jacket and the hollow shaft surface, cooled by automatic transmission fluid, [32], [33], [34].

The selected design is outlined in Fig. 1, a copper rotor CR-IM topology is employed: a stator with 36 slots and rotor with 50 bars topology is used for a 4-pole inner rotor configuration.

Starting from the vehicle performance the most suitable torque speed characteristic of the machine has been outlined, [35]. Hence a detailed optimization steps leading to this specific machine topology has been carried out and presented in [36]. The main motor dimension and performances, resulting from the design steps are resumed in Table II.

TABLE II
Main Motor Characteristics and Performance

Parameter	Unit	Value	Parameter	Unit	Valu e
Peak power	kW	307	Airgap length	mm	1
Peak torque	Nm	406	Active length	mm	150
Base speed	rpm	6000	Peak Specific. Power	kW/kg	5.6
Stator slots	-	36	Peak specific torque	Nm/kg	10.2
Pole pairs	-	2	Peak power density	kW/l	26.1
Rotor bars	-	50	Peak efficiency	%	96
Stator outer diam.	mm	190	Phase current	Arms	500
Rotor outer diam.	mm	118	Machine length	mm	270
Active weigth	kg	36			

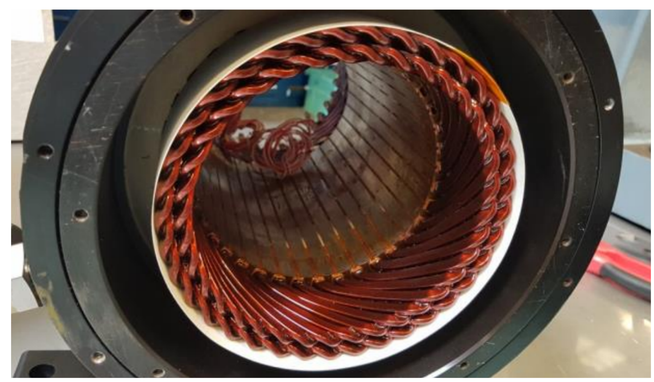

Fig. 2. Hairpin winding stator assembly and end winding detail for a four conductor/slot configuration (courtesy of Tecnomatic S.p.A.).

The hairpin implementation features four conductors/slots, the stator prototype is shown in Fig. 2. The current technology allows a number of conductors per slot up to 8 but, to the knowledge of the authors, work is pursued to push this limit to 16. The adoption of the transposition of the coil segments is needed to minimize AC copper losses. It means that each path formed by a series of connected coils must be placed in alternative slot layers on the motor periphery, [37].

III. Material Selection

The specific materials suitable for the CR-IM design in traction applications include electrical steels and copper alloys. Considering the high rotational speed, it is meaningful to select optimum materials for the CR-IM from the mechanical point of view, [38].

A. *Electrical Steel Selection*

For the stator and rotor laminations, different silicon–iron (SiFe) and cobalt–iron (CoFe) alloys can be considered. CoFe ensures higher saturation magnetization (above 2 Tesla) enabling higher power densities to be achieved. The actual value of saturation magnetization for CoFe depends on the annealing

TABLE III
CR-IM PERFORMANCE WITH VARIOUS ELECTRICAL STEEL GRADES

Property	***Unit***	***M235-35A***	***M290-50JKE***	***NO30-15***	***NO20-HS***
Magnetizing Current at 50Hz	Arms	162	160	169	168
Magnetizing Current at 400Hz	Arms	157	152	156	155
Max Torque at 50Hz/400Hz	Nm	370/350	370/350	370/350	370/350
Maximum Core Loss/ Total Loss	kW	0.98/31	1.6/31	0.75/31	0.84/31

temperature, time of annealing, and annealing atmosphere; in general, the better the mechanical characteristics of the annealed material, the lower the saturation magnetization. However, even when annealed to the optimum mechanical properties, the saturation magnetization of CoFe is still significantly higher than SiFe (around 20% higher). Materials of CoFe type, are significantly more expensive compared to SiFe laminations, hence the CoFe material is not considered for this project, [39].

Another important parameter when choosing the lamination material for CR-IM is the amount of the core losses generated in the lamination due to the relatively high fundamental (up to 1 kHz) and switching frequencies (up to 20 kHz). For a given frequency and flux density, the core losses are primarily influenced by the lamination thickness and the final annealing method. In general, the thinner the laminations, the lower the core losses. Electrical steels tailored specifically for high-frequency applications, as thin as 0.1 mm with very low core losses, are commercially available but again too expensive to CR-IM in EVs.

Four Non-Oriented (NO) electrical steel, silicon-iron type, have been considered for CR-IM. Tests on the steel samples have been performed on:

a) M235-35A (NO, fully-processed, thickness 0.35 mm)
b) M290-50JKE (NO, semi-processed, thickness 0.50 mm)
c) NO30-15 (NO, fully-processed, thickness 0.30 mm)
d) NO02-HS (NO, fully-processed, thickness 0.20 mm)

The performance comparison when considering various electrical steel grades is given in Table III. The M235-35A material was selected while the measured characteristics at 400 Hz referred to laser cutting techniques (with respect to the shear cutting) are used for performance evaluation and for further optimization.

Indeed, the frequency of 400 Hz represents the worst case in terms of torque capabilities, while the laser cutting process is adopted for prototyping to save on punching device building costs. However, the punching process must be considered for mass production since it allows cheaper cost per unit, but even lower specific losses and higher permeabilities with respect to the laser cut.

Fig. 3 represents the stress-strain characteristics obtained in the transverse and longitudinal directions for two specimens of different lengths (L-1, L-2). The parts of the curves of interest, that is the linear parts, are very close to each other, leading to

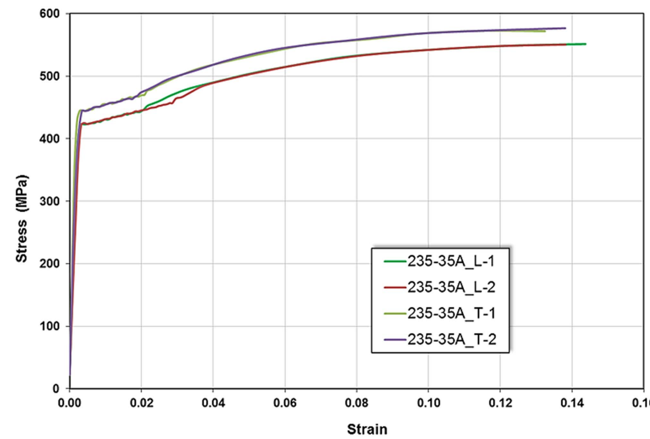

Fig. 3. Experimental test of stress-strain for M235-35A specimens of different length, measured on transverse and longitudinal directions.

TABLE IV
MECHANICAL PROPERTIES CALCULATED FROM TENSILE TESTS (M235-35A)

Property	**Unit**	**Catalogue data**		**Experimental value**	
		TD*	**RD***	**TD***	**RD***
Yield strength R_{p02}	MPa	430	-	444 - 444	423 - 424
Ultim. strength R_m	MPa	450	-	572 - 577	551 - 550
Elongation A_{80}	%	18	-	-	-
Elongation A_{50}	%	-	-	23.6 - 22.7	20.5 - 21.6

* TD: Transversal Direction; RD: Radial Direction (longitudinal).

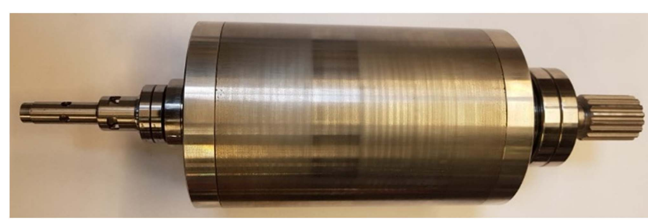

Fig. 4. Rotor prototype featuring cooling by shaft Spiral Groove.

similar mechanical properties in the two considered directions, as presented in Table IV. It can be noticed that the measurements are in accordance with the catalogue data.

B. Copper Alloys Selection

Two options are considered for the rotor cage of CR-IM: die-cast and fabricated copper alloys. Fig. 4 illustrates the rotor cage assembly for CR-IM design [40], [28].

Table V shows the possible options for fabricated copper alloys and the methods that can be used to securely fixing the rotor bars to the end-rings: the industry standard is to solder them together; alternatively, the rotor bars can be welded to the rings. A copper-silver alloy (CuAg0.04) was selected, showing a satisfactory trade-off between electrical and mechanical properties. For die-cast rotor solution, alloy Cu-ETP was selected. The difference between various solutions for the cage rotor material is related to the rotor equivalent resistance at 120 °C. Table VI summarizes the values used in the electromagnetic

TABLE V
FABRICATED COPPER ROTOR MATERIALS

Property	Unit	Bars and end-rings	Filler	
			Soldered	Welded
Material type	-	CuAg0.04	SAC305	Bercoweld K5
Tensile strength	MPa	338	29.7	220
Shear strength	MPa	-	27@20°C	17@20°C
Electrical resistivity	MΩ.m	1.702	10.4	5 - 6.67
Electrical conductivity	%IACS	101.3	16.6	25.8 - 34.4
Thermal conductivity	W/(mK)	388	58.7	120 - 145

TABLE VI
EQUIVALENT ROTOR RESISTANCE FOR VARIOUS COPPER ALLOYS

Copper cage type	Material	Rotor resistance @ 120°C - [Ω]
Die-cast	Cu ETP	0.01973
Fabricated: soldered end-ring	CuAg 0.04	0.02050
Fabricated: welded end-ring	CuAg 0.04	0.01902

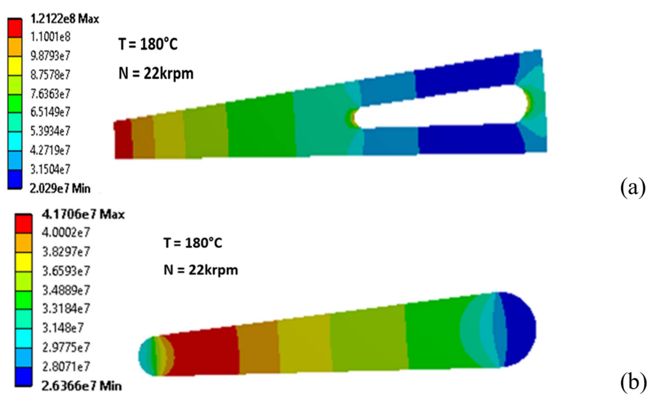

Fig. 5. Von Mises stress for inner rotor CR-IM, with (a) rotor core M235-35A steel and (b) copper bar (units in Pa).

analysis. Note the minor variation in CR-IM rotor resistance when considering die-cast or fabricated copper alloys.

Due to the high rotor speed, the mechanical integrity of the rotor core and the copper cage has been verified through Finite Element (FE) mechanical analysis performed at maximum operating temperature. The results in Fig. 5 confirm proper safety margins i.e., Von Mises stress is lower than the Yield stress reported in Tables IV and in VI. for the electrical steel and the copper respectively.

IV. ELECTROMECHANICAL PERFORMANCE

Extensive electromechanical analysis have been carried out to validate the performance of the proposed design.

Here the discussion focuses on the efficiency analysis of the Torque-Speed characteristics of the machine, detailing the losses

TABLE VII
MAIN OPERATING CONDITIONS FOR ELECTROMECHANICAL PERFORMANCE ESTIMATION

Parameter	Unit	Value	Parameter	Unit	Value
Maximum Current	Arms	500	Motor Temperature	°C	120
Maximum speed	rpm	20000	PWM frequency	kHz	20
DC Bus Voltage	V	720	Base Speed	krpm	6000

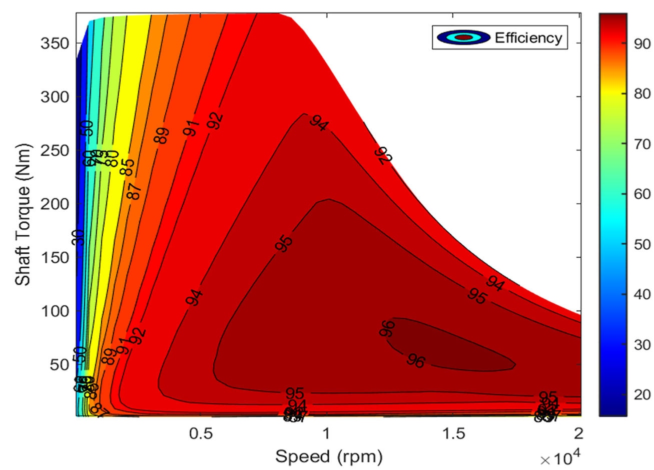

Fig. 6. Efficiency map for the CR-IM, with M235-35A steel.

in the hairpin windings due to the fundamental frequencies and harmonics of the phase current.

Concerning the motor performance validation, a Maximum Torque Per Ampere control strategy (MTPA) is selected below the base speed where high torque is the priority, [41]. Then, a suitable field weakening strategy is applied above the base speed where the highest possible power is demanded, and voltage is a limitation. The main operating conditions are collected in Table VII.

The loss components included in the efficiency estimations are DC and AC stator copper losses, rotor copper losses, stator/rotor core losses, windage and stray load contribution, while bearing loss and PWM effects are neglected.

The complete efficiency map is reported in Fig. 6. A large, high efficiency operating zone can be noticed over a wide speed range for low to medium torque levels.

The highest losses are observed in the peak power operations (10–15 krpm) where the combined effect of peak current, core saturation, and high frequency produces peak losses also in the electrical steel material (Fig. 7), nevertheless the efficiency is maintained above 90%. The total losses are strongly affected by the copper losses, confirmed by the trend of the isolines reported in Fig. 8, proportional to the torque (current) levels.

The presented total losses and related efficiency maps are computed without accounting for the PWM feed. PWM harmonics do not significantly affect the iron losses as explained in [42], but they may affect copper losses in the hairpin windings due the large section of flat wires. This loss component is estimated by adopting a transient voltage-fed FE model approach as in

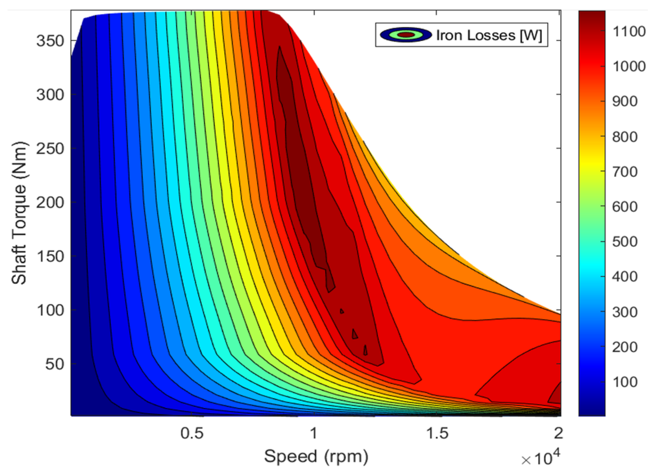

Fig. 7. Map of the core losses in the torque speed characteristics of the motor using the selected M235-35A material.

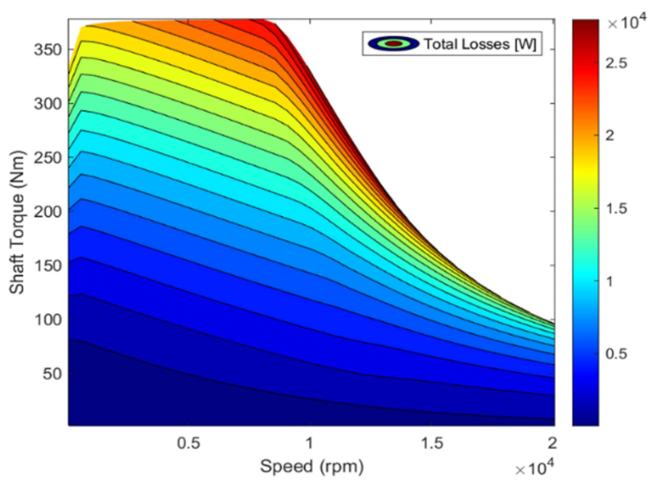

Fig. 8. Map of the total losses of the CR-IM.

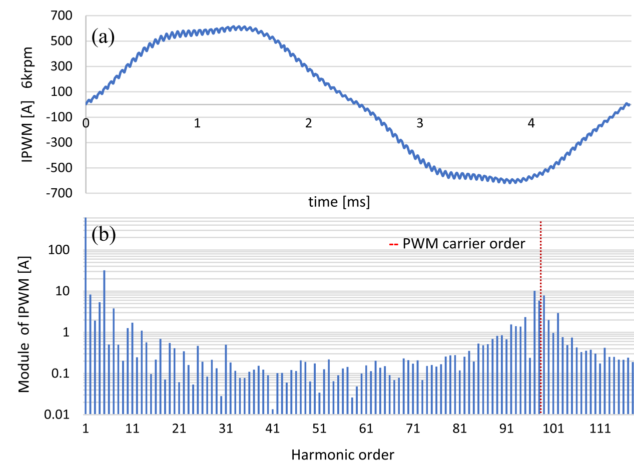

Fig. 9. Simulated phase current at steady state operation (370 Nm, 6 krpm and 204.8 Hz fundamental frequency, 20 kHz PWM carrier): (a) current waveform; (b) module of the harmonics.

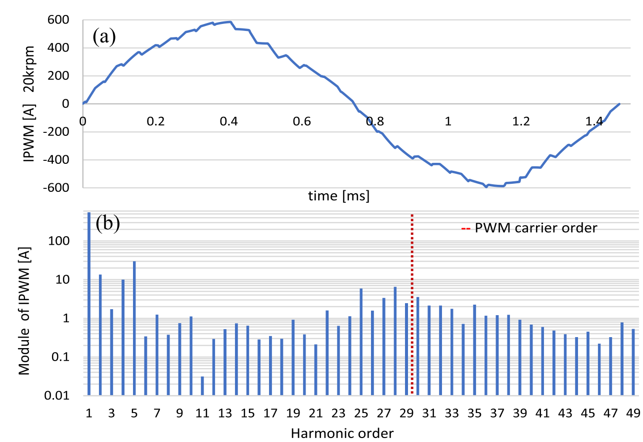

Fig. 10. Simulated phase current at steady state operation (96 Nm, 20 krpm and 680.3 Hz fundamental frequency, 20 kHz PWM carrier): (a) current waveform; (b) module of the harmonics.

[43], where the feeding voltage is generated by a voltage source inverter and a target control strategy is applied. A complete 3D analysis is unfeasible due to the computational effort and the many iterations required, hence a 2D analysis has been preferred and end-windings contribution computed by proper parameters. Even with a 2D approach the analysis is computationally intensive (a dense mesh is needed for wires) and can be carried out only in validation steps. Recent studies aim to investigate simplified models to account for PWM losses even in preliminary design and optimization steps, [31].

The voltage-fed FE analysis adopts the controlled phase current, including its harmonic content, to evaluate the losses generated by the PWM feed. Figs. 9 and 10 reports respectively the phase current in two meaningful working points: 370 Nm 6 krpm (base speed, max torque) and 90 Nm 20 krpm (max speed); the time domain waveform and the frequency harmonic modulus are reported. The related losses distribution in the flat wires can be analyzed in steady state condition, here the results related to the maximum speed (maximum fundamental frequency) is shown in Fig. 11.

The rotor field has a negligible effect on the eddy current losses in the stator winding, as already envisaged in [29], [44], [45]. Analytically, by using the current harmonic content [21], the ohmic losses in the frequency domain can be computed by superposition principle [46], with not negligible contribution due to the PWM because of the high frequency and amplitude of the current harmonics.

Hence, the DC and AC Joule losses are computed by considering the harmonic content in Figs. 9 and 10 and reported in Fig. 12. By repeating the analysis for different working point all over the torque speed characteristics, it is possible to compute the total winding losses due to the PWM feed as reported in Fig. 13 and to refine accordingly the efficiency map (Fig. 14).

The efficiency map is strongly affected in the torque levels from low to medium, speed values from medium to high; where in comparison with Fig. 6, the 96% peak efficiency is not achievable anymore. Preliminary results on experimental efficiency are reported in Table VIII. (test bench limited to 80 kW–12.000 rpm) and compared to the Sinusoidal feeding in Fig. 6, and PWM

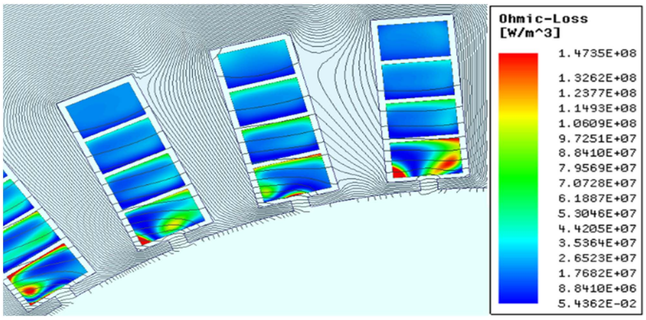

Fig. 11. Ohmic-Losses distribution in the hairpin at maximum speed operation (96 Nm, 20000 rpm, 20 kHz PWM modulation): isolines represents magnetic field density, colorzones represent Ohmic-losses density.

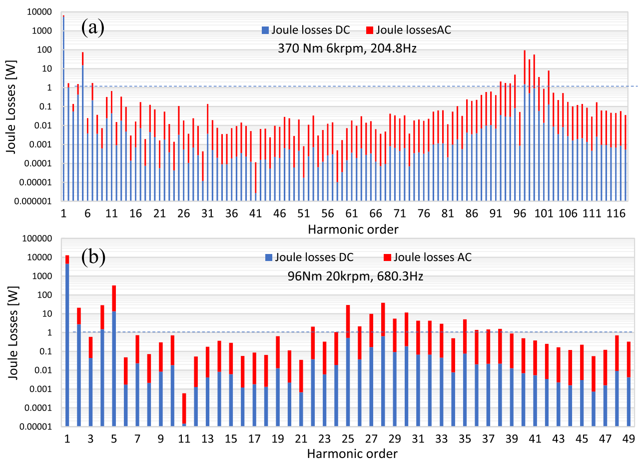

Fig. 12. Frequency domain representation of the Ohmic-losses contribution at steady state operation: (a) 6 krpm, 204.8 Hz fundamental frequency; (b) 20 krpm, 680.3 Hz fundamental frequency, 20 kHz PWM carrier).

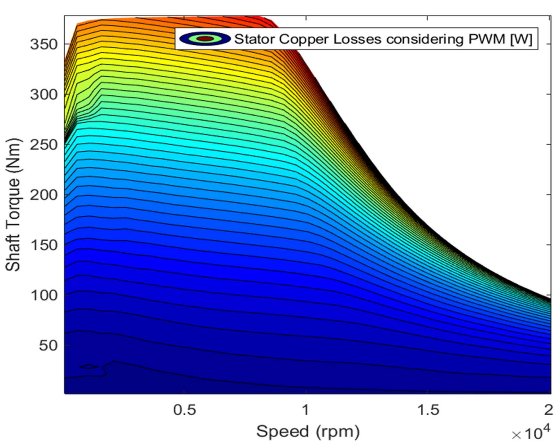

Fig. 13. Total winding losses including the contributions of PWM harmonics.

feeding in Fig. 14. The efficiency computed by including PWM feeding is closer to the real motor efficiency.

V. Thermal Performance

In induction machines, most of the loss components are of electrical resistive Joule type and located in the stator winding

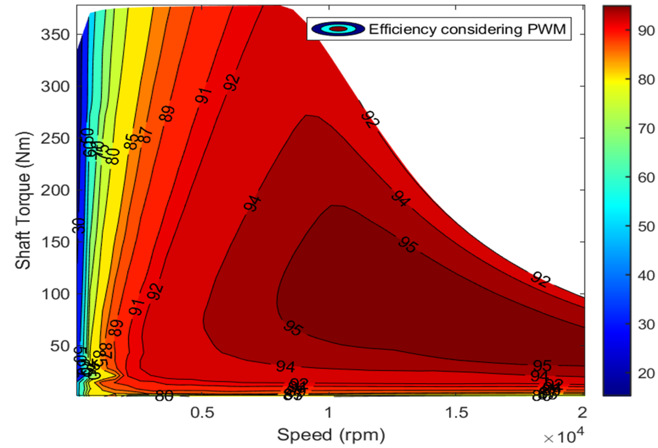

Fig. 14. Efficiency map accounting for PWM contributions on the stator copper losses.

TABLE VIII
Computed Efficiency Considering Sinusoidal Feed vs PWM Feed and Experimental Data

Torque [Nm]	Speed [rpm]	Efficiency - Sinus. Feed	Efficiency PWM feed	Efficiency - Experimental
185.5	4000	92.1	91.68	89.2
95	8000	95.6	95.2	94.5
80	9000	95.7	94.38	94.7
19	12000	94.3	92.38	91.2
60	12000	96.2	95.2	94.7

and rotor cage. The iron losses may represent a more significant heat source only at higher speed operation. Also, the mechanical losses must be considered. From the temperature levels point of view, the critical points to be considered are described below.

A. Bearings

This motor components represents the most frequent cause of failure in IM. Bearings in motors are considered mechanical devices. However, they do possess electrical properties that affect their lifetime. Bearings are subject to currents that can cause significant damage if neglected. There are two classes of currents that can increase wear on the bearings. The first class is low-frequency and the second class is high-frequency.

For low-frequency bearing currents, published experimental results showed that the shaft voltage threshold is approximately 300 – 500 mV. A solution to this type of bearing currents is to use insulated bearings, which will break the circuit path preventing the flow of the current. High-frequency bearing currents occur when an inverter-fed controller is used because of the high dv/dt.

The following solutions to limit bearing currents are in place. These include:

- one or two insulated bearings;
- hybrid or ceramic bearings;
- filter on inverter to reduce/eliminate common mode voltage;
- lower switching frequency;
- insulated coupling between motor and load.

The rate of failure due to low or high frequency bearing currents is not known or not sufficient data is published for a correct assessment. Mechanical failure of bearings is known to lead to more than 50% of the overall electric motor failure. Motor bearings within an electric motor can be damaged from improper handling and storage, improper installation, misalignment, improper lubrication, start/stop processes, contamination, overhung loads and of course overheating.

At high-speed bearings heats up due to their own friction losses, in the range of 200 W–800 W each one, depending on the bearing type and assembly layout. Moreover, the shaft drains the heat from the rotor and can increase bearing temperature. An accurate analysis of the shaft cooling must include the bearings and their operating temperature verification.

B. Stator Winding

This is limited by the insulation class, typically Class 180 °C (H). Higher levels can be used by either using more expensive insulation classes, e.g., 220 °C, 240 °C or considering that each insulation class can withstand higher temperature levels than the standard, but with impact on the insulation life. Each 10 °C temperature increase, leads to faster aging of the insulation, halving the life of a machine.

Winding insulation has a certain life and if subjected to overheating, the insulation can be aged rapidly. 55% of the insulation faults are due to the overheating, [47]. Therefore, a proper electromagnetic/thermal design of the motor is necessary and a proper insulation class selection [48], [49].

C. Rotor Cage

This has an indirect effect on the IM thermal response. Typically, a copper cage can operate safely at higher temperatures > 200 °C. However, the high temperature will affect the rotor lamination insulation and can create circulating currents between lamination sheets. Also, the heat generated by the rotor cage losses will be extracted via conduction and propagated to the shaft and bearings.

D. Envisioned Cooling Systems

For the thermal CS of IM, we consider two possible solutions as detailed in the following [47], [50], [51], [52].

1) Water Jacket and Shaft Spiral Groove (WJSG): An housing Water Jacket (WJ) and shaft Spiral Groove (SG) CSs are coupled in parallel, using Ethylene Water Glycole (EWG) mixture as a coolant (Fig. 15). This type of cooling is used in the Tesla Model S60D and the Audi e-tron traction motors. This CS was optimized with the continuous torque maximization at low speed as a target. The variables include the housing thickness, the WJ channel dimensions (width and height), the shaft channel thickness and the flow rate distribution between the two flow paths. The main constraints concern the continuous power at maximum speed (≥ 70 kW) and the maximum pressure drop in the housing WJ (≤10 kPa). Table IX provides the characteristics obtained from the optimization process. Note that the pressure drop in the shaft is not specified. This quantity depends on the turbulences between the two coaxial cylinders, namely the dimensions and speed of the rotor, and can only be calculated from extensive Computational Fluid Dynamics (CFD) analysis. However, the rotor dimensions are in line with existing technologies, so the cooling efficiency and manufacturability are guaranteed.

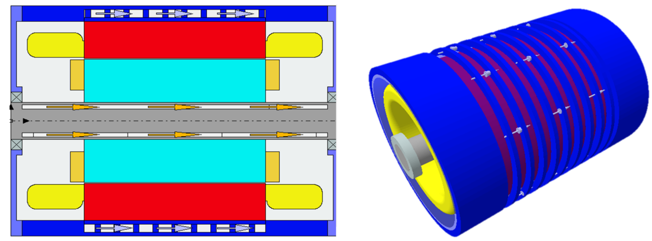

(a) Axial view (b) 3D view

Fig. 15. Motor cooling system (1) based on housing Water Jacket (WJ) and shaft Spiral Groove (SG).

TABLE IX
MAIN CHARACTERISTICS OF COOLING SYSTEMS

Parameter	Unit	SYSTEM (1) WJ+SG		SYSTEM (2) WJ+OS	
		WJ	**SG**	**WJ**	**SG**
Fluid inlet temperature	°C	75 (EWG)	75 (EWG)	90 (ATF)	90 (ATF)
Fluid flow rate	l/min	5.75	4.25	6	2
Pressure drop	kPa	10.42	-	15	-
Channel number	-	10	1	10	1

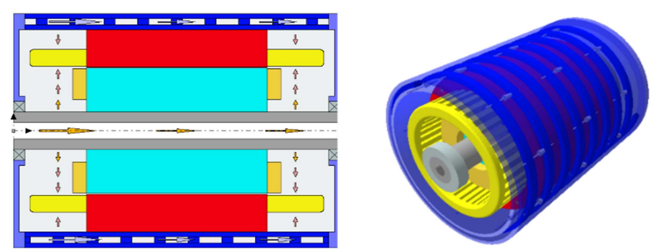

(a) Axial view (b) 3D view

Fig. 16. Motor cooling system (2) based on Water Jacket (WJ) and Oil Spray (OS) cooling of the end-windings.

2) Water Jacket and Oil Spray (WJOS): An housing water jacket (WJ) and hollow shaft CSs are coupled in parallel, with Oil Spray (OS) through nozzles placed on the shaft and the housing as shown in Fig. 16, using Automatic Transmission Fluid (ATF) as a coolant [51], [52]. For comparison, the second option with oil spray was designed using the same external envelope as the first cooling design, larger channels, no optimization was performed in this case. Its characteristics are given in Table IX. Note that the pressure drop in the shaft is not specified because this quantity is very sensitive to the fluid velocity though the nozzles which varies with the rotational effects. Extensive CFD analysis are required for an accurate prediction. Alternatively, the nozzles dimensions were adjusted to limit the fluid velocity and the resulting pressure drop. The machine's thermal behaviour was evaluated in transient peak load operation for 30 seconds at base speed, without any potting material for end-windings. The estimated winding maximum

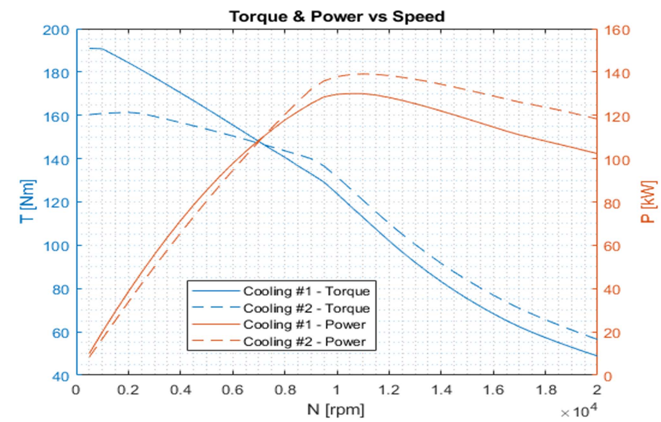

Fig. 17. Comparison between motor continous performance considering cooling systems (1) and (2).

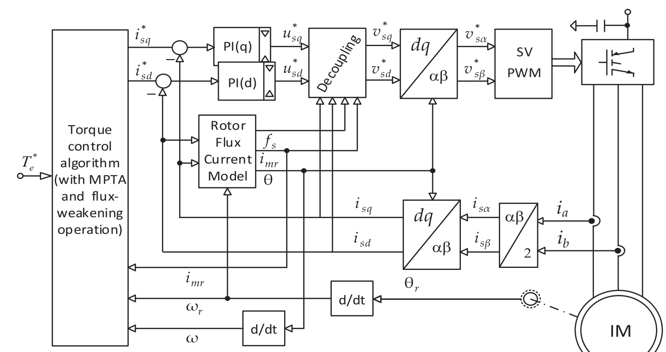

Fig. 18. Reference RFOC scheme adopted in the dynamic analysis.

temperature is 120 °C for CS (WJSG) where a value of 195 °C was found for CS (WJOS).

Fig. 17 shows the comparison between continuous performance of the inner rotor topology using the CSs. It was assumed that maximum acceptable temperatures are 180 °C for both the stator winding and rotor cage. Note the advantages of CS (WJSG) at low speed, high torque operation, where the optimization was focused. The better performance of the CS (WJOS) at high-speed depends on the increased rotational effects on the oil splash and spray technique, aiding the extraction of the high-speed copper losses due to AC components. Globally, it can be concluded that higher torque density is obtained by the CS (WJSG), while higher power density is reached with CS (WJOS). System (WJSG) has been prototyped and preliminary experimental tests confirms the integrity of the rotor cooling up to 20000 rpm.

VI. Control Strategy and Dynamic Performance

In previous sections motor performance has been analyzed by ideal steady state supply, nevertheless the control strategy dynamically regulates the motor AC voltages and currents through the power converter. A detailed validation of the real machine behaviour must not exclude the analysis of the control strategy and the dynamic machine performance. Indeed, the control strategy is commonly designed and tuned by using lumped parameters models of the machines.

Nevertheless, high power density machines parameters are strongly affected by saturation effects, cross-coupling and high frequency effects (i.e., eddy currents) or efficiency oriented control strategies, [53], [54], [55], [56], [57], [58].

These effects can be modeled through the so-called transient FE method co-simulation, a time-consuming and computationally intensive technique where the FE model of the machine is solved on each time-varying output value of the control strategy, [59].

The following aspects can be evaluated:

- Accurate voltage limit of the machine;
- Required bandwidth of the control strategy;
- Minimum PWM frequency required;
- Torque ripple introduced by the control aspects;
- Effectiveness of the control strategy.

The control strategy considered for this analysis is the widely used Field-Oriented Control (FOC). Rotor Flux-Oriented Control (RFOC) is preferred for IMs, as it allows an independent regulation of machine's flux for a more effective control, [60]. The *d*-axis current (i.e., the linkage rotor flux) is kept constant at its rated value until the rated speed (constant-torque region), then it is reduced (field-weakening region) due to voltage limits, the detail of the control scheme is reported in Fig. 18.

A torque controller manages the machine operation by imposing the $d-q$ current references depending on the speed. Therefore, Flux and torque quantities are imposed by the respective $d-q$ current components (that in the following test case are driven directly for demonstration purposes). The stator windings are fed by a current-regulated PWM voltage-source inverter. Proportional-Integral (PI) current regulators are used, with output limitation and anti-wind-up features, their outputs represent the voltage reference. A decoupling block has been included at the outputs of the current regulators to improve the control dynamics [61], [62].

The control implementation requires the knowledge of the time-varying rotor flux position $\vartheta(t)$ and amplitude $\Psi_r(\mathrm{i}_{mr}(t))$, as a function of the magnetizing current $\mathrm{i}_{mr}(t)$. In fact, the rotor flux position allows the transformations between the stator $\alpha-\beta$ and the rotor flux $d-q$ components, while the rotor flux amplitude serve the flux regulator to be controlled. The rotor flux current model allows to estimate them considering the classical equivalent IM model in the rotor-flux aligned reference frame $d-q$, [61].

An accurate knowledge of the parameters involved in the rotor flux current model and in the decoupling equations are needed to accurately control the IM. Rated motor parameters are reported in Table X. However, especially the rotor parameters are difficult to be measured and they are easy to drift (due to the temperature, eddy currents and saturation effects mainly). The effects of modelling mismatches can be outlined by the transient FE method co-simulation approach and a meaningful test case for the IM drive is proposed. This method allows in principle to estimate the complete powertrain (vehicle) dynamic performance, down to the detailed commutation of the power electronics. Nevertheless, the today computation technologies

TABLE X
MOTOR PARAMETERS AT RATED OPERATING POINT (340 NM, 6000 RPM)

Parameter	Symbol	Value
Stator Resistance	R_s	0,0175 Ω
Rotor Resistance	R_r	0.0196 Ω
Stator leakage inductance	L_s	0,0478 mH
Rotor leakage inductance	L_r	0,0962 mH
Magnetizing inductance	M	1,071 mH
Number of pole pairs	p	2
Moment of Inertia	J	0,0197 kgm^2

Rotor quantities are referred to stator side.

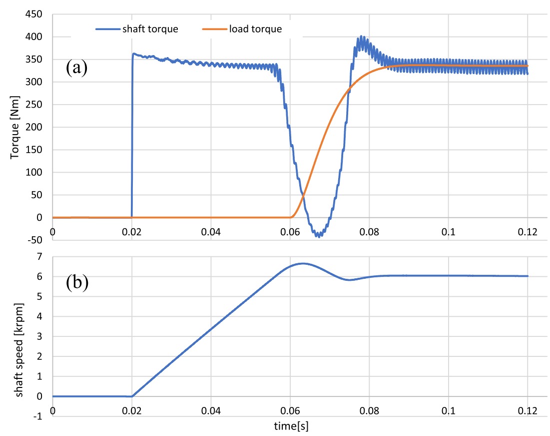

Fig. 19. Dynamic Performance analysis: motor acceleration, load insertion and steady state operation. Shaft and torque, (a) and shaft speed, (b).

allow to investigate only few cycles of the fundamental frequencies in detail. To achieve reasonable simulation time the power electronics has been modelled as a transfer function and a proper test case is analyzed to explore the three meaningful operating condition resumed in the following points.

1) Magnetization: (t = 0.5 ms for 0.02 s) where a step variation of the d-current reference at from zero to the rated value builds-up the flux in the machine.
2) Acceleration: (up to 0.06 s) where a step variation of the q-current reference from zero to rated value makes the motor accelerate up to rated speed. Rated torque is required due to properly tuned acceleration and inertia.
3) Steady state: (after 0.08 s) rated load torque is applied (with a smooth 2nd order dynamics) to reach steady state operations at constant speed.

Even if properly reduced inertia is used, every transient analysis requires several hours to be computed on a custom simulation server. Fig. 19 reports the resulting torque and speed in the dynamic operation, during the acceleration step a slight but evident torque reduction can be noticed when the speed increase. This effect is accounted to the detuning of the control algorithm, that affects in detail the decoupling computation and the synchronous speed estimation, both based on constant parameters. The deterioration of the control performance increases the voltage required by the motor up to the voltage limitation with effects on the resulting torque. The result is that the motor may require higher battery voltage to reach the expected performance.

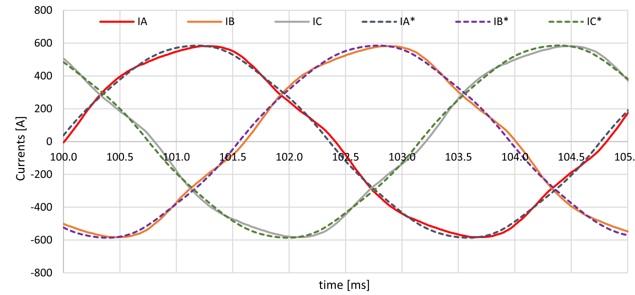

Fig. 20. Dynamic performance analysis: detail of the motor phase currents in steady state operations.

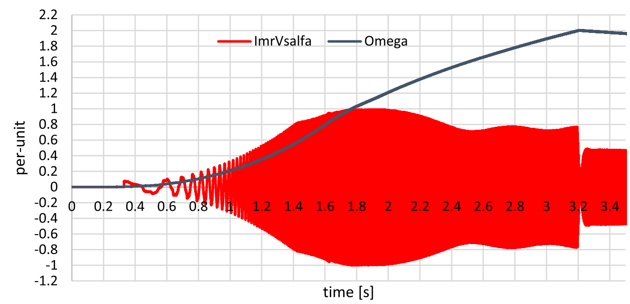

Fig. 21. Experimental no-load acceleration from zero to 12000 rpm (2 p.u.): α-axis reference voltage $v^*_{s\alpha}$ (p.u.) and mechanical rotor speed (p.u.).

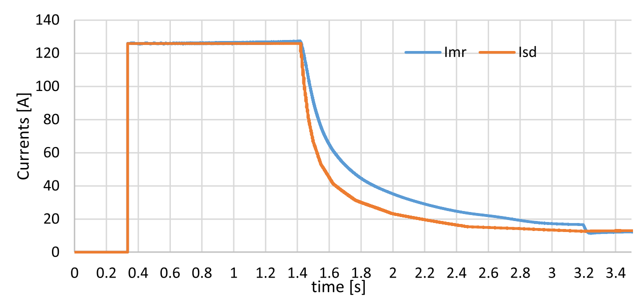

Fig. 22. Experimental Dynamic Performance: magnetizing current i_{mr} and d-axis reference current i^*_{sd} in an acceleration from zero to 12000 rpm (2 p.u.) with no-load.

The discussed issues also affect the steady state operation, where the controlled currents fail to follow the sinusoidal reference (Fig. 20). Current harmonics are introduced by the poor current control, affecting affect the average torque, the torque ripple, and the efficiency. This effect become relevant in high-speed machines, where operating conditions often reach the voltage limits. In this specific case the dynamic analysis confirms the effectiveness of the design with slight performance deviations, to be eventually compensated by an accurate control tuning or adaptive control strategies, [54], [55], [56].

Hence, the transient FE method co-simulation approach make possible to set the MPTA and the flux-weakening trajectories in the control algorithm with more accuracy than lumped parameter models, [59]. In Figs. 21 and 22 an experimental acceleration up to the speed of 12000 rpm, maximum testbed capability, is proposed and allows to evaluate how the control imposes a flux-weakening strategy and therefore a reduction of the magnetizing current $\mathrm{i}_{mr}(t)$ when the speed overcome the rated value for which the maximum available voltage is reached.

VII. Conclusion

The potentialities of induction machines in EV traction systems are investigated in this paper. The discussion details the motor topology selection, the materials evaluation, the cooling methods, and the performance estimation for the design validation. Particular attention has been paid to ensure the industrial feasibility for large mass production scenarios at low manufacturing costs.

The electrical steel grade is recommended to remain non-oriented, fully processed silicon iron, 0.35 mm thickness, with possible grades: M235-35A, M250-35A, M270-35A or equivalent.

The copper cage can be built using two technologies, die-cast and fabricated, with similar performance. The choice between modes of manufacturing the rotor cage depends on the production volume and investments.

The hairpin winding is a preferred technology for such application, due to the reduced copper loss and manufacturing suitable for automation. AC copper loss needs accurate analysis to account for the contribution given by high order harmonics.

Dual cooling system with forced liquid convection for both the stator and rotor are necessary for any induction motor used in EV traction. Only one cooling system, be this on the stator or rotor assembly will lead to early thermal failure of either the bearings or stator windings, respectively.

Accurate dynamic analysis is suggested for performance verification in high-speed, high-power-density powertrains, where machine parameters are strongly affected by the operating point. Therefore, performance degradation can be introduced by the controller due to low control dynamics, mismatch in machine parameters or poor control tuning.

In conclusion, the present study shows that the Copper Rotor Induction Motor technology can represent an effective avenue for the development of RE-free electric powertrains.

Acknowledgment

The authors would like to acknowledge and thank their colleagues from RINA – Centro Sviluppo Materiali, Tecnomatic, Aurubis, Breuckmann and R13 Technology for their contributions and useful discussions.

References

[1] M. Popescu, N. Riviere, G. Volpe, M. Villani, G. Fabri, and L. di Leonardo, "A copper rotor induction motor solution for electrical vehicles traction system," in *Proc. IEEE Energy Convers. Congr. Expo.*, 2019, pp. 3924–3930.

[2] C. Liu, K. T. Chau, C. H. T. Lee, and Z. Song, "A critical review of advanced electric machines and control strategies for electric vehicles," *Proc. IEEE*, vol. 109, no. 6, pp. 1004–1028, Jun. 2021, doi: 10.1109/JPROC.2020.3041417.

[3] S. Cai, J. L. Kirtley, and C. H. T. Lee, "Critical review of direct-drive electrical machine systems for electric and hybrid electric vehicles," *IEEE Trans. Energy Convers.*, vol. 37, no. 4, pp. 2657–2668, Dec. 2022, doi: 10.1109/TEC.2022.3197351.

[4] W. Cai et al., "Review and development of electric motor systems and electric powertrains for new energy vehicles," *Automot. Innov.*, vol. 4, pp. 3–22, 2021.

[5] C. Liu, K. T. Chau, C. H. T. Lee, and Z. Song, "A critical review of advanced electric machines and control strategies for electric vehicles," *Proc. IEEE*, vol. 109, no. 6, pp. 1004–1028, Jun. 2021.

[6] S. Cai, J. L. Kirtley, and C. H. T. Lee, "Critical review of direct-drive electrical machine systems for electric and hybrid electric vehicles," *IEEE Trans. Energy Convers.*, vol. 37, no. 4, pp. 2657–2668, Dec. 2022.

[7] B. Ballinger et al., "The vulnerability of electric-vehicle and wind-turbine supply chains to the supply of rare-earth elements in a 2-degree scenario," *Sustain. Prod. Consumption*, vol. 22, pp. 68–76, 2020.

[8] European Commission, "Critical materials for strategic technologies and sectors in the EU - A foresight study," 2020.

[9] Z. Q. Zhu and D. Howe, "Electrical machines and drives for electric, hybrid, and fuel cell vehicles," *Proc. IEEE*, vol. 95, no. 4, pp. 746–765, Apr. 2007.

[10] I. Boldea, L. N. Tutelea, L. Parsa, and D. Dorrell, "Automotive electric propulsion systems with reduced or no permanent magnets: An overview," *IEEE Trans. Ind. Electron.*, vol. 61, no. 10, pp. 5696–5711, Oct. 2014.

[11] J. D. Widmer, R. Martin, and M. Kimiabeigi, "Electric vehicle traction motors without rare earth magnets," *Sustain. Mater. Technol., Elsevier*, vol. 3, pp. 7–13, 2015.

[12] I. Husain et al., "Electric drive technology trends, challenges, and opportunities for future electric vehicles," *Proc. IEEE*, vol. 109, no. 6, pp. 1039–1059, Jun. 2021.

[13] Z. Wang, T. W. Ching, S. Huang, H. Wang, and T. Xu, "Challenges faced by electric vehicle motors and their solutions," *IEEE Access*, vol. 9, pp. 5228–5249, 2020.

[14] C. S. Goli, M. Manjrekar, S. Essakiappan, P. Sahu, and N. Shah, "Landscaping and review of traction motors for electric vehicle applications," in *Proc. IEEE Transp. Electrific. Conf. Expo*, 2021, pp. 162–168.

[15] J. Goss, M. Popescu, and D. Staton, "A comparison of an interior permanent magnet and copper rotor induction motor in a hybrid electric vehicle application," in *Proc. Int. Electric Mach. Drives Conf.*, 2013, pp. 220–225,.

[16] J. L. Kirtley, F. Schiferl, D. T. Peters, and E. F. Brush, "The case for induction motors with die-cast copper rotors for high efficiency traction motors," SAE Tech. Paper 2009-01-0956, 2009.

[17] R. Tiwari and A. K. Bhardwaj, "Analysis of induction motor with die-cast rotor," *Int. J. Innov. Res. Elect., Electron., Instrum. Control Eng.*, vol. 2, no. 6, pp. 1–7, Feb. 2014.

[18] S. T. Varghese, K. R. Rajagopal, and B. Singh, "Design and development of rotor quality test system for die-cast copper rotors," *IEEE Trans. Ind. Appl.*, vol. 54, no. 3, pp. 2105–2114, May/Jun. 2018, doi: 10.1109/TIA.2018.2792418.

[19] A. Bárdos, C. Walczer, Z. Kéri, and I. Selmeczi, "Copper rotor technology for high efficiency motors," in *Vehicle and Automotive Engineering 2*, K. Jármai and B. Bolló, Eds., Lecture Notes in Mechanical Engineering, Berlin, Germany: Springer, 2018.

[20] S. Yamamoto, "Overview of the latest research and development for copper die-cast squirrel-cage rotors," in *Proc. IEEE Int. Power Electron. Conf.*, 2018, pp. 1949–1954.

[21] R. Thomas, H. Husson, L. Garbuio, and L. Gerbaud, "Comparative study of the Tesla model S and Audi e-Tron induction motors," in *Proc. 17th Int. Conf. Elect. Mach., Drives Power Syst. (ELMA)*, Sofia, Bulgaria, Jul. 2021.

[22] E. A. Grunditz and T. Thiringer, "Performance analysis of current BEVs based on a comprehensive review of specifications," *IEEE Trans. Transp. Electrific.*, vol. 2, no. 3, pp. 270–289, Sep. 2016.

[23] Online database. Accessed: Jul. 2019. [Online]. Available: www.evspecifications.com

[24] Y. Zhao, D. Li, T. Pei, and R. Qu, "Overview of the rectangular wire windings AC electrical machine," *CES Trans. Elect. Mach. Syst.*, vol. 3, no. 2, pp. 160–169, Jun. 2019, doi: 10.30941/CESTEMS.2019.00022.

[25] A. Riedel et al., "Challenges of the hairpin technology for production techniques," in *Proc. IEEE 21st Int. Conf. Elect. Mach. Syst.*, 2018, pp. 2471–2476.

[26] S. Guercioni, "Method and fixture for twisting end portions of bar conductors, in particular for bar windings of electric machines," U.S. Patent No 9,520,762, Dec. 13, 2016.

[27] Inside the HVH Hybrid Motor – Technical insights on Remy's "Off-the-Shelf" Hybrid Motor Solutions, White Paper, Remy Electric Motors, Pendleton, IN, USA, 2009.

[28] S. Jurkovic, K. M. Rahman, J. C. Morgante, and P. J. Savagian, "Induction machine design and analysis for general motors e-assist electrification technology," *IEEE Trans. Ind. Appl.*, vol. 51, no. 1, pp. 631–639, Jan./Feb. 2015.

[29] C. Du-Bar and O. Wallmark, "Eddy current losses in a hairpin winding for an automotive application," in *Proc. IEEE XIII Int. Conf. Elect. Mach.*, 2018, pp. 710–716.

[30] G. Berardi and N. Bianchi, "Design guideline of an AC hairpin winding," in *Proc. IEEE XIII Int. Conf. Elect. Mach.*, 2018, pp. 2444–2450.

[31] L. Di Leonardo, M. Popescu, and M. Villani, "Eddy-current losses evaluation in hairpin wound motor fed by PWM inverter," in *Proc. IEEE 46th Annu. Conf. Ind. Electron. Soc.*, 2020, pp. 943–948.

[32] M. Popescu, D. A. Staton, A. Boglietti, A. Cavagnino, D. Hawkins, and J. Goss, "Modern heat extraction systems for power traction machines—A review," *IEEE Trans. Ind. Appl.*, vol. 52, no. 3, pp. 2167–2175, May/Jun. 2016.

[33] K. Bennion and G. Moreno, "Convective heat transfer coefficients of automatic fluid jets with implications for electric machine thermal management," presented at InterPACK, 2015. [Online]. Available: https://www.osti.gov/servlets/purl/1225460

[34] M. Popescu, J. Goss, D. A. Staton, D. Hawkins, Y. C. Chong, and A. Boglietti, "Electrical vehicles—Practical solutions for power traction motor systems," *IEEE Trans. Ind. Appl.*, vol. 54, no. 3, pp. 2751–2762, May/Jun. 2018.

[35] A. Credo, M. Villani, G. Fabri, and M. Popescu, "Adoption of the synchronous reluctance motor in electric vehicles: A focus on the flux weakening capability," *IEEE Trans. Transp. Electrific.*, vol. 9, no. 1, pp. 805–818, Mar. 2023.

[36] N. Riviére, M. Villani, and M. Popescu, "Optimisation of a high speed copper rotor induction motor for a traction application," in *Proc. IEEE 45th Annu. Conf. Ind. Electron. Soc.*, 2019, pp. 2720–2725.

[37] N. Bianchi and G. Beradi, "Analytical approach to design hairpin winding in high performance electric vehicle motors," in *Proc. IEEE Energy Convers. Congr. Expo.*, 2018, pp. 4398–4405.

[38] D. Gerada, A. Mebarki, N. L. Brown, C. Gerada, A. Cavagnino, and A. Boglietti, "High-speed electrical machines: Technologies, trends and developments," *IEEE Trans. Ind. Electron.*, vol. 61, no. 6, pp. 2946–2959, Jun. 2014.

[39] P. Ramesh and N. C. Lenin, "High power density electrical machines for electric vehicles—Comprehensive review based on material technology," *IEEE Trans. Magn.*, vol. 55, no. 11, Nov. 2019, Art no. 0900121.

[40] M. Caprio, V. Lelos, J. Herbst, S. Manifold, and H. Jordon, "High strength induction machine, rotor, rotor cage end ring and bar joint, rotor end ring, and related methods," U.S. Patent 7 504 756, Mar. 17, 2009.

[41] A. Popov, V. Popova, I. Gulyaev, and F. Briz, "Dynamic response of FOC induction motors using MTPA considering voltage constraints," in *Proc. IEEE 26th Int. Workshop Electric Drives: Improvement Efficiency Electric Drives (IWED)*, 2019, pp. 1–5.

[42] A. Boglietti, A. Cavagnino, and A. M. Knight, "Isolating the impact of PWM modulation on motor iron losses," in *Proc. IEEE Ind. Appl. Soc. Annu. Meeting*, 2008, pp. 1–7.

[43] L. Di Leonardo, F. Parasiliti, M. Tursini, and M. Villani, "Transient analysis of PM synchronous motor drives by finite element model co-simulation," in *Proc. IEEE 39th Annu. Conf. Ind. Electron. Soc.*, 2013, pp. 6834–6840.

[44] P. H. Mellor, R. Wrobel, and N. McNeill, "Investigation of proximity losses in a high speed brushless permanent magnet motor," in *Proc. IEEE Conf. Rec. Ind. Appl. Conf. 41st IAS Annu. Meeting*, 2006, pp. 1514–1518.

[45] P. B. Reddy, T. M. Jahns, and T. P. Bohn, "Modeling and analysis of proximity losses in high-speed surface permanent magnet machines with concentrated windings," in *Proc. IEEE Energy Convers. Congr. Expo.*, 2010, pp. 996–1003.

[46] A. Tessarolo, M. Bortolozzi, and M. Mezzarobba, "On the validity of the harmonic superposition principle for computing rotor eddy current losses in permanent magnet machines," in *Proc. IEEE XXth Int. Conf. Elect. Mach.*, 2012, pp. 1369–1373.

[47] G. C. Stone, I. Culbert, E. A. Boulter, and H. Dhirani, "Electrical insulation for rotating machines: Design, evaluation, aging, testing, and repair," in *IEEE Press Series on Power Engineering*, 2nd ed. Hoboken, NJ, USA: Wiley, 2014.

[48] P. Mancinelli, S. Stagnitta, and A. Cavallini, "Qualification of hairpin motors insulation for automotive applications," *IEEE Trans. Ind. Appl.*, vol. 53, no. 3, pp. 3110–3118, May/Jun. 2017.

[49] G. Berardi, S. Nategh, and N. Bianchi, "Inter-turn voltage in hairpin winding of traction motors fed by high-switching frequency inverters," in *Proc. IEEE XIV Int. Conf. Elect. Mach.*, 2020, pp. 909–915.

[50] M. Rosu et al., *Multiphysics Simulation by Design for Electrical Machines, Power Electronics and Drives*. Piscataway, NJ, USA: IEEE Press, 2018.

[51] S. H. Swales et al., "Oil cooled motor/generator for an automotive powertrain," U.S. Patent Application #US 8169110 B2, May 01, 2012.

[52] L. Fedoseyev and E. M. Pearce Jr, "Rotor assembly with heat pipe cooling system," U.S. Patent Application # 2014/0368064 A1, May 03, 2016.

[53] J. C. Moreira and T. A. Lipo, "Modelling of saturated AC machines including air gap flux harmonic components," in *Proc. IEEE Conf. Rec. 1990 Ind. Appl. Soc. Annu. Meeting*, 1990, vol. 1, pp. 343–349, doi: 10.1109/IAS.1990.152162.

[54] D. Bispo, L. Martins, Neto, J. T. de Resende, and D. A. de Andrade, "A new strategy for induction machine modeling taking into account the magnetic saturation," *IEEE Trans. Ind. Appl.*, vol. 37, no. 6, pp. 1710–1719, Nov./Dec. 2001, doi: 10.1109/28.968182.

[55] W. Bischof, B. Chatterjee, M. Boesing, M. Hennen, and R. Kennel, "Modeling inverter-fed three-phase squirrel-cage induction machines including spatial and temporal harmonics," in *Proc. IEEE Int. Electric Mach. Drives Conf.*, 2017, pp. 1–8, doi: 10.1109/IEMDC.2017.8002150.

[56] A. A. Ahmed, B. K. Koh, and Y. I. Lee, "A comparison of finite control set and continuous control set model predictive control schemes for speed control of induction motors," *IEEE Trans. Ind. Inform.*, vol. 14, no. 4, pp. 1334–1346, Apr. 2018, doi: 10.1109/TII.2017.2758393.

[57] S. K. Sahoo, T. Bhattacharya, and M. Aravind, "A synchronized sinusoidal PWM based rotor flux oriented controlled induction motor drive for traction application," in *Proc. IEEE 28th Annu. Appl. Power Electron. Conf. Expo.*, 2013, pp. 797–804, doi: 10.1109/APEC.2013.6520301.

[58] B. Gallert, G. Choi, K. Lee, X. Jing, and Y. Son, "Maximum efficiency control strategy of PM traction machine drives in GM hybrid and electric vehicles," in *Proc. IEEE Energy Convers. Congr. Expo.*, 2017, pp. 566–571.

[59] L. Di Leonardo, M. Popescu, M. Tursini, and M. Villani, "Finite elements model co-simulation of an induction motor drive for traction application," in *Proc. IEEE 45th Annu. Conf. Ind. Electron. Soc.*, 2019, pp. 1059–1065.

[60] D. W. Novotny and T. A. Lipo, *Vector Control and Dynamics of AC Drives*. London, U.K.: Oxford Univ. Press, 1996.

[61] R. D. Lorenz, T. A. Lipo, and D. W. Novotny, "Motion control with induction motors," *Proc. IEEE*, vol. 82, no. 8, pp. 1215–1240, Aug. 1994.

[62] L. di Leonardo, M. Popescu, G. Fabri, and M. Tursini, "Performance evaluation of an induction motor drive for traction application," in *Proc. IEEE 45th Annu. Conf. Ind. Electron. Soc.*, 2019, pp. 4360–4365.

Mircea Popescu (Fellow, IEEE) received the M.Eng. and Ph.D. degrees in electrical engineering from the "Politehnica" University of Bucharest, Bucharest, Romania, in 1984 and 1999, respectively, and the D.Sc. degree in electrical machines from Aalto University, Espoo, Finland in 2004. He is currently a Principal Product Specialist with Ansys, Sheffield, U.K. He has more than 35 years of engineering experience. He was with the Helsinki University of Technology (now Aalto University), SPEED Laboratory, University of Glasgow, Glasgow, U.K. and Motor Design Ltd, Wrexham, U.K. He has authored or coauthored more than 150 peer reviewed papers. Dr. Popescu was the recipient of three IEEE best paper awards. Dr. Popescu is an Associate Editor for IEEE Transactions on Industry Applications and *IET Electric and Power Applications* journal. He was an Officer of the IEEE Industry Application Society Electrical Machines Committee 2010–2017 and Prominent Lecturer for IAS Region 8, 2014-2016.

Lino Di Leonardo was born in Pescina, Italy, in 1986. He received the M.S. degree in computer and automation engineering and the Ph.D. degree in electrical and information engineering from the University of L'Aquila, L'Aquila, Italy, in 2010 and 2014, respectively. In particular, the Ph.D. thesis concerns dynamic co-simulation analysis of motor drives. In 2012, he was a Visiting Ph.D. Student with the École Supérieure d'Ingénieurs en Électrotechnique et Électronique d'Amiens (ESIEE-Amiens). He was an Assistant Researcher with the Department of Industrial and Information Engineering and Economics, University of L'Aquila. His research interests include the designing, modeling, and simulation of electrical machines focusing on permanent-magnet synchronous motors, dual-rotor permanent magnet induction machine, reluctance motors, finite-element and multi-physics integrated simulation tools, and DSP-based real-time simulation platforms.

Giuseppe Fabri (Member, IEEE) received the M.S. degree in electronic engineering and the Ph.D. degree in electrical and information engineering from the University of L'Aquila, L' Aquila, Italy, in 2009 and 2013, respectively. He is currently an Assistant Professor with the Department of Industrial and Information Engineering and Economics, University of L'Aquila. In 2013, he was a Research Fellow with the Swiss Federal Institute of Technology, Lausanne, Switzerland. He designed and tested different development tools, test benches, and demonstrators to aid innovative electric drives' design and validation process. His research interests include development, control, and test of electrical motors and drives mainly related to fault-tolerant systems for aircraft and automotive applications, design of power electronics, DSP-based control platforms, and the implementation of motion control algorithms for ac drives.

Giuseppe Volpe (Member, IEEE) received the B.Sc. and M.Sc. degrees in electrical engineering from the University of Cassino, Cassino, Italy, in 2013 and 2015, respectively, and the Ph.D. degree in 2019. In 2015, he was with a European funded project joining Shenyang University of Technology, Shenyang, China. His research interests include the design and performance prediction of electrical machines for automotive and motorsport applications. He has worked several years with Motor Design Ltd., Wrexham, U.K., focusing on designing electrical machines for hybrid and electric cars and motorbikes. He is currently with Magna Powertrain, Troy, MI, USA, leading the advanced engineering eMotor team.

Nicolas Riviere received the master's degree engineering degree in electrical engineering from Toulouse University, Toulouse, France, in 2014, where he specialized in electromechanical energy conversion and advanced mechatronics. For three years, he was with the Laboratory on Plasmas and Energy Conversion (LAPLACE Lab.), Toulouse, where he worked on the design of a high speed permanent magnet synchronous machine for an automotive application. He is currently a Senior Engineer with Motor Design Ltd., Wrexham, U.K., where he is mainly involved in consultancy projects, and U.K. and European funded projects.

Marco Villani received the M.S. degree in electrical engineering from the University of L'Aquila, L'Aquila, Italy, in 1985. In 1990, he was Research Fellow with the University of Dresden, Dresden, Germany and with the Nagasaki University, Nagasaki, Japan, in 1995. Since 2000, he took the responsibility of several national and international research projects and contracts between the University of L'Aquila and industrial partners. He is currently an Associate Professor of electrical machines design and electric systems for mobility. His research interests include modeling and design of electrical machines, high-efficiency induction motors, design of PM synchronous motors and synchronous reluctance motors for industrial, automotive, and aerospace applications.